PHOTONICS Research

Blue perovskite single-mode lasing in a rubidium lead bromide microcubic cavity

Bo Li,[1,2] Wangqi Mao,[1,2,5] Shuang Liang,[3] Yifeng Shi,[4] Hongxing Dong,[2,6] and Long Zhang[1,2,7]

[1]Department of Optics and Optical Engineering, University of Science and Technology of China, Hefei 230026, China
[2]Key Laboratory of Materials for High-Power Laser, Shanghai Institute of Optics and Fine Mechanics, Chinese Academy of Sciences, Shanghai 201800, China
[3]State Key Laboratory of Precision Spectroscopy, School of Physics and Electronic Science, East China Normal University, Shanghai 200241, China
[4]School of Microelectronics, Shanghai University, Shanghai 201800, China
[5]e-mail: mwangqi@mail.ustc.edu.cn
[6]e-mail: hongxingd@siom.ac.cn
[7]e-mail: lzhang@siom.ac.cn

Received 24 February 2023; revised 17 April 2023; accepted 21 April 2023; posted 21 April 2023 (Doc. ID 488164); published 30 May 2023

Lead halide perovskite microlasers have shown impressive performance in the green and red wavebands. However, there has been limited progress in achieving blue-emitting perovskite microlasers. Here, blue-emitting perovskite-phase rubidium lead bromide ($RbPbBr_3$) microcubes were successfully prepared by using a one-step chemical vapor deposition process, which can be utilized to construct optically pumped whispering gallery mode microlasers. By regulating the growth temperature, we found that a high-temperature environment can facilitate the formation of the perovskite phase and microcubic morphology of $RbPbBr_3$. Notably, blue single-mode lasing in a $RbPbBr_3$ microcubic cavity with a narrow linewidth of 0.21 nm and a high-quality factor (~2200) was achieved. The obtained lasing from $RbPbBr_3$ microlasers also exhibited an excellent polarization state factor (~0.77). By modulating the mixed-monovalent cation composition, the wavelength of the microlaser could be tuned from green (536 nm) to pure blue (468 nm). Additionally, the heat stability of the mix-cation perovskite was better than that of conventional $CsPbBr_3$. The stable and high-performance blue single-mode microlasers may thus facilitate the application of perovskite lasers in blue laser fields.

https://doi.org/10.1364/PRJ.488164

1. INTRODUCTION

Miniaturized and high-quality coherent light sources with excellent lasing performance have potential applications in several fields, including optical communication, sensing, computing, and imaging [1–9]. In this regard, lead halide perovskites are promising materials for the preparation of microlasers owing to their unique properties, which include a high optical gain (~3200 cm^{-1}, comparable with that of single-crystal GaAs), tunable bandgap, large absorption coefficient, high quantum yield, and low density of defect states [10–15]. Since the first amplified spontaneous emission of $CH_3NH_3PbX_3$ perovskite thin films was achieved by Xing *et al.* [16], optically pumped perovskite microlasers have been successfully fabricated and have demonstrated impressive performance in the green and red regions [17–23]. Despite such remarkable progress, the sky blue and even pure blue, which represent two important wavebands for perovskite laser applications, remain underexplored.

Blue perovskite lasers can be primarily realized via component engineering with halide doping and dimensional modulation based on the quantum confinement effect [24,25]. The former involves the realization of perovskite blue emissions from mixed halogens with chlorine–bromine doping; however, this method often requires the addition of large amounts of chlorine, leading to severe phase separation of perovskite materials under the action of external fields and poor excitation performance and laser stability [26–28]. The latter is based on 3D perovskites, which can be produced by adding organic ammonium salts or other organic long-chain ligands to form layered quasi-2D perovskites or quantum dots. However, the addition of large amounts of long-chain organic ligands leads to severe optical losses and a high excitation threshold of the laser cavity [29,30]. Consequently, the preparation of efficient and stable blue perovskite materials has become crucial for the application of perovskite lasers in blue laser fields.

Notably, the A-site cations of lead halide perovskites ($APbX_3$) are primarily limited to three candidates: methylammonium (MA^+), formamidine (FA^+), and cesium (Cs^+), and these are determined by size and structural constraints to fit into the space of lead halide perovskite lattices. Recent studies have revealed that Rb^+ can replace Cs^+ and produce a key

impact on the optoelectronic and physicochemical properties of lead halide perovskites [31–34]. Although certain studies have focused on Rb^+ doping, most studies have focused solely on Rb^+ trace doping [30,32]. Notably, the blueshift in the luminescence wavelength resulting from Rb^+ trace doping is limited. Moreover, synthesizing highly Rb^+ doped $CsPbBr_3$ perovskites or even $RbPbBr_3$ perovskites at room temperature is often difficult, further hindering the applications of perovskite microlasers in the waveband from sky blue to pure blue. Our early work realized perovskite-phase $RbPbBr_3$ microspheres and analyzed mechanism of the perovskite–nonperovskite phase transition in 2019 [35]. However, the crystallinity and stability of the $RbPbBr_3$ microspheres based on thermal annealing treatment are unsatisfactory. To improve crystal quality and simplify the preparation process for perovskite-phase $RbPbBr_3$, the growth kinetic processes and phase transition mechanism still require further study.

In this study, we successfully fabricated all-inorganic perovskite-phase $RbPbBr_3$ microcubic cavities (MCCs) by a one-step chemical vapor deposition method. Further, by regulating the growth temperature, we found that a high-temperature environment facilitated the formation of the perovskite phase and microcubic morphology of $RbPbBr_3$. The MCCs with strong blue light emission at a wavelength of 463.5 nm featured smooth and regular cubic geometries, which acted as natural microlaser cavities. Blue single-mode lasing was observed in a $RbPbBr_3$ MCC under femtosecond (fs) laser pumping with a laser threshold of 6.76 $\mu J/cm^2$, a high-quality factor of about 2200, and a high linear polarization state factor (~0.77). By adjusting the ratio of monovalent cations, a tunable single-mode laser output (468–536 nm) was achieved in $Rb_xCs_{1-x}PbBr_3$ microcubic lasers. In addition, $Rb_xCs_{1-x}PbBr_3$ MCCs presented more stable light emission from 293 to 413 K and demonstrated higher heat stability than conventional $CsPbBr_3$. Thus, the developed stable and high-performance blue single-mode microlasers may facilitate the applications of perovskite lasers in blue laser fields.

2. METHOD

A. Synthesis and Structural Characterization of $RbPbBr_3$ MCCs

Unlike top-down fabricated devices, which have relatively rough boundaries, bottom-up synthesized perovskites can be in the form of single crystals, with naturally smooth cavity boundaries. In this study, $RbPbBr_3$ MCCs were synthesized using dual-source chemical vapor deposition. The chemical vapor deposition system consisted of a horizontal tube furnace with a maximum heating temperature of 1473 K, a gas flow meter, and a quartz tube. The vapor source was composed of $PbBr_2$ powder (99.0%) and rubidium bromide (RbBr, 99.6%) powder at a molar ratio of 1:1. All reagents were used without further purification and purchased from Sigma-Aldrich and Mackulin. To prepare the $RbPbBr_3$ MCCs, we placed the $PbBr_2$ and RbBr powders upstream and at the center of the quartz tube, respectively, and a mica boat (12 mm × 18 mm × 2 mm) downstream. High-purity nitrogen was introduced into the quartz tube at a constant flow rate of 3 L/h. The tube furnace was then rapidly heated to 973 K and held at this temperature for 30 min; and then the quartz tube was cooled to room temperature. Field-emission scanning electron microscopy (SEM; Auriga S40, Zeiss, Oberkochen, Germany) and high-resolution transmission electron microscopy (TEM; Talos F200X) were used to characterize the morphology, composition, and single-crystal structures of the prepared $RbPbBr_3$ microcubes.

B. Lasing Characterization of $RbPbBr_3$ MCCs

A single isolated $RbPbBr_3$ MCC was selectively excited using a 400 nm fs-laser, which was obtained through a BBO crystal from the amplifier laser source (Libra, Coherent, B40 fs, 10 kHz); this laser was then focused on a 2 μm diameter spot through the 100× objective to excite individual $RbPbBr_3$ microcubes uniformly. $RbPbBr_3$ MCCs were measured in ambient atmosphere using a confocal microphoto-luminescence system (LabRAM HR Evolution). At the end of the signal collection optical circuit, we placed a half-wave plate and a polaroid to obtain the maximum and minimum photoluminescence (PL) intensities. By rotating the half-wave plate (0°–180°), we obtained a complete angular polarization diagram. The PL lifetime of $RbPbBr_3$ MCCs is measured by FLRM300 (Time-Tech Spectra, LLC). Temperature-dependent measurements were performed on a Research Supertran ST-500 system equipped with a two-input, four-control loop cryogenic temperature controller (Model 22C, Cryocon), which is a continuous-flow research cryostat.

3. RESULT AND DISCUSSION

A. Characterizations of $RbPbBr_3$ MCCs

The $RbPbBr_3$ MCCs were grown via a one-step chemical vapor deposition method using RbBr and $PbBr_2$ powders as source materials and mica as a substrate in a tube furnace. A typical SEM image of the synthesized samples is depicted in Fig. 1(a). As shown, the $RbPbBr_3$ MCCs were dispersed on the mica with diameters ranging from 0.4 to 2.2 μm; their dimensions were in an ideal size regime for realizing single-mode lasing. The upper-right inset of Fig. 1(a) clearly presents the perfect cubic morphology and smooth surface of a $RbPbBr_3$ MCC, which is an ideal candidate for optically resonant microcavity. The electron diffraction pattern of the $RbPbBr_3$ MCC is depicted in Fig. 1(b), which exhibits the perfect single-crystal structure of the $RbPbBr_3$ MCC. The inset of Fig. 1(b) shows a TEM image of the $RbPbBr_3$ MCC, confirming its regular cubic morphology from clear contrast. To evaluate the chemical composition of the $RbPbBr_3$ MCCs, energy-dispersive X-ray spectroscopy (EDX)-based elemental mapping images of Rb, Pb, and Br are depicted in Fig. 1(c). The foregoing three elements appear to be uniformly distributed in the same $RbPbBr_3$ MCC.

The SEM images in Fig. 1(d) indicate that the morphologies of the $RbPbBr_3$ MCCs vary at different positions on the mica substrate. In particular, owing to varying deposition temperatures, these microcavities exhibit spherical, cubic, and in-between morphologies. The results indicate that microcubes have clear edges and regular smooth cubic structures, whereas the surfaces of the microspheres and in-between morphologies appear to be rough. Based on the SEM images captured at

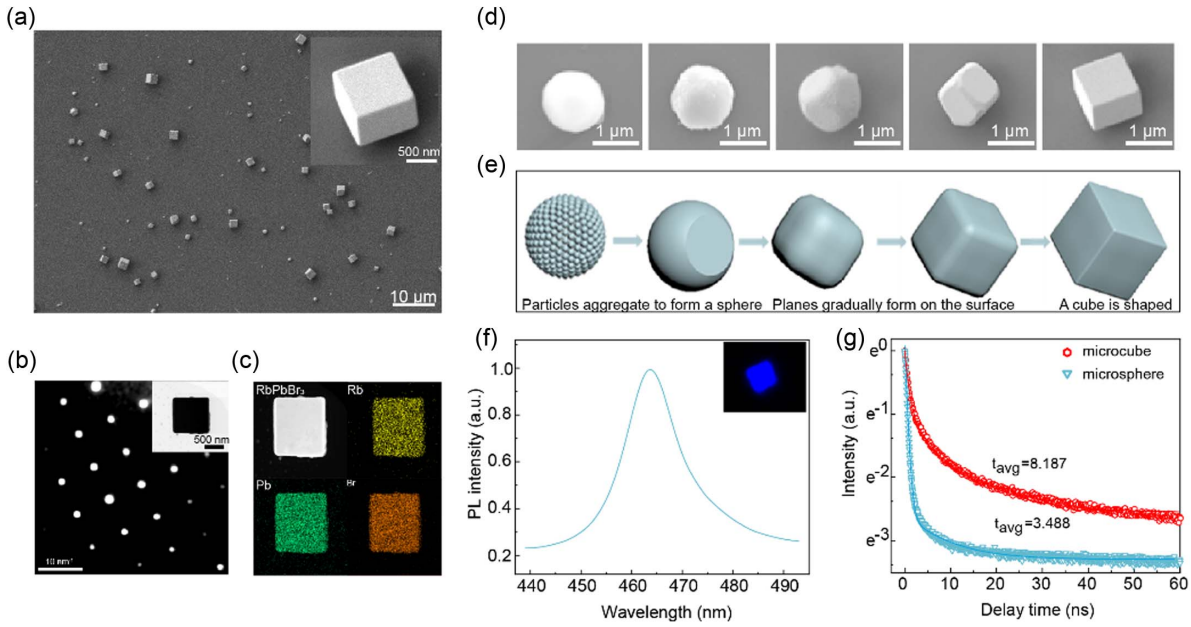

Fig. 1. Characterizations of $RbPbBr_3$ MCCs. (a) Typical SEM images of the $RbPbBr_3$ MCCs. Inset: magnified image of an individual $RbPbBr_3$ MCC. (b) Selected area electron diffraction pattern of an individual $RbPbBr_3$ MCC. Inset: TEM image of a $RbPbBr_3$ MCC. (c) EDX elemental mapping of a $RbPbBr_3$ MCC, displaying its uniform composition. (d) SEM images of several $RbPbBr_3$ microstructures located at different growth positions. (e) Shape evolution process from a microsphere to a microcube. (f) PL spectrum of as-grown $RbPbBr_3$ MCCs excited using a 405 nm continuous wave laser at room temperature. Inset: PL image of an individual $RbPbBr_3$ microcube. (g) Time-resolved PL curves of a $RbPbBr_3$ microcube (red line) and a $RbPbBr_3$ microsphere (blue line).

different stages of growth, one can infer that the microcubes were gradually transformed from microspheres. The shape of crystal would tend to grow into a closed polyhedron during growth, which is the fundamental property of crystal growth [36,37]. The shape of the crystal reflects its internal laws. Generally, surface energy of different crystallographic planes is different, for instance, $\gamma(111) < \gamma(100) < \gamma(110)$. Remarkably, this is not inconsistent with the lowest surface energy of spherical structures. Because stable single crystal structures are usually the closest-packed structure such as face-centered cubic (FCC) closest-packed, body-centered cubic (BCC), and shexagonal closest-packed (HCP) structures. Therefore, the closest-packed crystal structure could be more stable compared with the spherical single crystal. During crystal growth, owing to the varying deposition temperatures of these microcavities, growth rates were also different. If the overall growth rate is slow, spherical shape at low crystallinity is more favorable, and reactant particles aggregate into spherical structure owing to surface tension. As analyzed above, the nearly spherical structure with high surface energy is unstable. When the overall growth rate is fast, sufficient energy allows full crystal growth and particles aggregate to form planes on the surfaces of the single crystal spheres. The growth rate of the anisotropic single crystal $RbPbBr_3$ gets faster along a specific crystal direction. $RbPbBr_3$ microcubes could be realized by controlling the growth time. The process that microspheres transform into dense microcubes is shown in Fig. 1(e). Generally, microcubes and microspheres are WGM cavities. The resonant mode of a spherical microcavity WGM is sensitive to the surface morphology. Typically, scattering from a rough surface affects the quality of the microcavity [38]. As analyzed above, microspheres collect particles and form irregular planes, leading to the creation of defects. Such microspheres exhibit more optical losses. Compared with microspheres, well-crystallized and smooth microcubes are better candidates for WGM cavities.

Further, PL spectra of the $RbPbBr_3$ MCCs were recorded at room temperature [Fig. 1(f)], and a strong peak at 463.5 nm with a full width at half-maximum (FWHM) of 12.5 nm was obtained. The upright images in Fig. 1(f) show far-field PL images of a $RbPbBr_3$ microcube that was excited at a low pump intensity, and these images clearly indicate that the $RbPbBr_3$ MCC emitted blue fluorescence. Figure 1(g) shows PL decay curves of a microsphere and a microcube. These curves were well fitted with a bi-exponential function, and the average fluorescence lifetime τ_{avg} of the microcube (8.178 ns) is much longer than that of the microcube (3.488 ns). The results reveal that the microcubes have significantly longer lifetimes than the microspheres, which supports our inference regarding the better crystallinity and stability of the microcubes.

B. Single-Mode Lasing Characteristics of $RbPbBr_3$ MCC Lasers

Next, optically pumped lasing experiments were performed at room temperature. As schematically presented in Fig. 2(a), a 400 nm fs-laser was used as the excitation light source. The laser spot covered an entire $RbPbBr_3$ MCC to ensure homogeneous excitation. The $RbPbBr_3$ MCC acted as a gain medium and optical resonant microcavity. At a high pump intensity, the optical gain balanced or exceeded the optical losses, and blue lasing was observed. The blue square path in the Fig. 2(a) indicates light propagation inside the MCC.

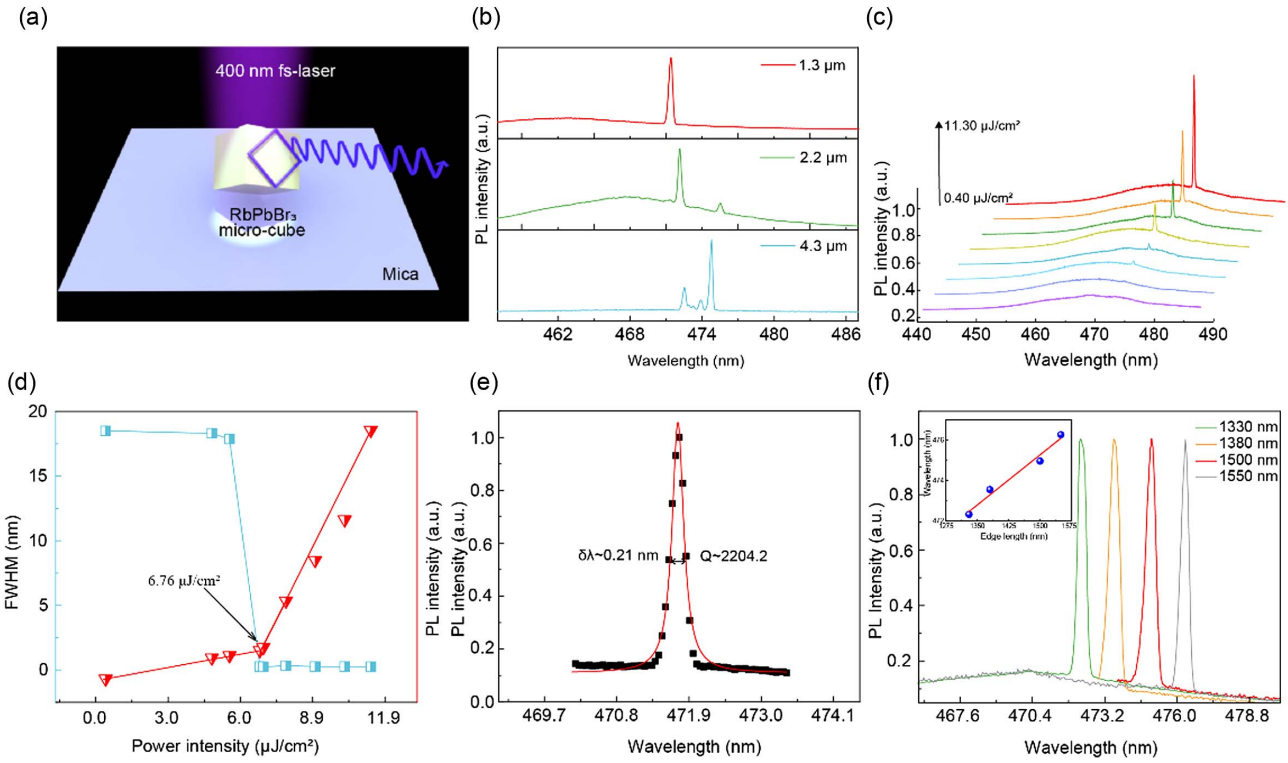

Fig. 2. Single-mode lasing characteristics of $RbPbBr_3$ MCC lasers. (a) Individual $RbPbBr_3$ MCC pumped by a 400 nm fs-laser (approx. 40 fs, 10 kHz). (b) Resonant optical modes of $RbPbBr_3$ MCCs with different sizes. Single-mode lasing was achieved, and the spacing between two adjacent modes decreased with increasing cavity size. (c) Excitation power-dependent lasing spectra obtained from a single $RbPbBr_3$ MCC. (d) Output intensity (red) and FWHM (blue) as a function of the pump intensity. The integrated lasing intensity as a function of the pumping density obtained from the $RbPbBr_3$ MCC indicates that the lasing threshold P_{th} is 6.76 $\mu J/cm^2$. (e) Lorentz fitting of a lasing oscillation mode at 471.7 nm, yielding an ultrasmall linewidth of ≈2200, corresponding to a high Q-factor of ≈2200. (f) Single-mode lasing spectra of four $RbPbBr_3$ MCCs with different sizes. Inset: relationship between the wavelength of single-mode lasing and the sizes of $RbPbBr_3$ MCCs.

We performed lasing emission analysis for $RbPbBr_3$ MCCs with different edge lengths of the cubic cavity [Fig. 2(b)]. The mode space and energy centers of the lasing peaks could be controlled by adjusting the size of the $RbPbBr_3$ MCCs. With a reduction in the edge length of the cavity from 4.3 to 1.3 μm, a transition from multimode lasing to single-mode lasing was achieved.

Figure 2(c) presents the typical excitation-power-dependent PL spectra of a single $RbPbBr_3$ MCC with an edge length of approximately 1.2 μm. A single broad emission peak resulting from spontaneous emission could be observed at ~467 nm with an FWHM of $\delta\lambda \sim 18.4$ nm when the pump intensity was below the threshold of 6.76 $\mu J/cm^2$. When the pump intensity exceeded the threshold, a single sharp peak abruptly appeared above the spontaneous emission background, and its intensity increased drastically with a further increase in the pump intensity. Importantly, no other resonant peaks were observed in this process. A clear evolution from spontaneous to stimulated emission was observed in the $RbPbBr_3$ MCC, indicating the achievement of single-mode lasing. Simultaneously, a broadening of the FWHM of the lasing peak (0.21–0.28 nm) was observed with an increase in the excitation power. This could be attributed to the high injected carrier density, which may have induced a variation in the refractive index of the materials and thus lead to a shift in cavity modes during the dynamic process of stimulated emission of pulsed lasers. In particular, single-mode lasing at 471.7 nm was observed for the $RbPbBr_3$ MCC with an edge length of ~1.2 μm.

To further confirm the lasing action, the peak emission intensity and FWHM versus excitation power are displayed in Fig. 2(d); here, the output-integrated intensity suggests a distinct transition from PL to lasing. The transition from spontaneous emission to stimulated emission occurs at 6.76 $\mu J/cm^2$, and the FWHM plummets from 17.86 to 0.27 nm at this point, which can be considered as the lasing threshold P_{th}. Figure 2(e) presents single-mode lasing at approximately 471.7 nm, and a Lorentz curve with $\delta\lambda \sim 0.21$ nm is used to fit these plots. According to the following equation,

$$Q = \lambda/\delta\lambda, \tag{1}$$

where λ is the peak center wavelength and $\delta\lambda$ is the peak width. The quality factor Q of single-mode lasing at 471.7 nm was calculated to be about 2200. Notably, the cubic shapes of $RbPbBr_3$ MCCs make them ideal WGM candidates for total internal reflection and for ensuring lower optical losses. Therefore, the achievement of single-mode lasing with a high Q-factor can be primarily attributed to the excellent optical resonant cavity structures. Further, the lasing behavior of $RbPbBr_3$ MCCs was investigated to clarify the influence of the microcavity size on the lasing properties. Notably, the

wavelength tunability of a laser is one of the most important parameters for practical applications. Generally, the resonant modes of a WGM microcavity can be expressed as [37,39,40]

$$2\sqrt{2}L/(\nu/n) = \lambda, \tag{2}$$

where L denotes the length of the edge of a cubic cavity, λ denotes the wavelength of the resonant peak, and ν and n denote the mode order and refractive index of the medium, respectively. Figure 2(f) presents the single-mode lasing spectra recorded for different $RbPbBr_3$ MCCs with different sizes. As the length of the edge increased from 1330 to 1550 nm, the single-mode lasing wavelength redshifted from 472.2 to 476.3 nm. According to Eq. (2), we can infer that, despite changes in the cavity length, only one mode is present in the gain interval, which implies that the mode order remains unchanged. This further implies that ν/n is a constant value, and L and λ are linearly proportional, as indicated in the inset of Fig. 2(f).

C. Polarization Properties of $RbPbBr_3$ MCC Lasers

Interestingly, microlasers with linear polarization demonstrate a wide range of practical applications in signal detection, fundamental research, and display technologies. To study the polarization anisotropy of the microlasers, the laser emission spectra as a function of the rotation angle (θ) with respect to a linear polarizer below and above the lasing threshold were recorded for comparison. As depicted in Figs. 3(a) and 3(b), minimal changes in the PL intensity were observed with variations of θ, indicating a low polarization ratio below the threshold value. However, the lasing action above the threshold [Figs. 3(c) and 3(d)] was strongly polarized. We set the θ of the maximum PL intensity at 0°. When θ is an integral multiple of 90°, it shows spontaneous emission. However, when θ is an integral multiple of 180°, linearly polarized lasing is realized. This polarized laser has also been observed in other lasers in previous studies [41]. This polarization characteristic may be related to the anisotropic optical gain of the crystal. Notably, polarization anisotropy can be quantitatively reflected based on the polarization state factor, defined as [42]

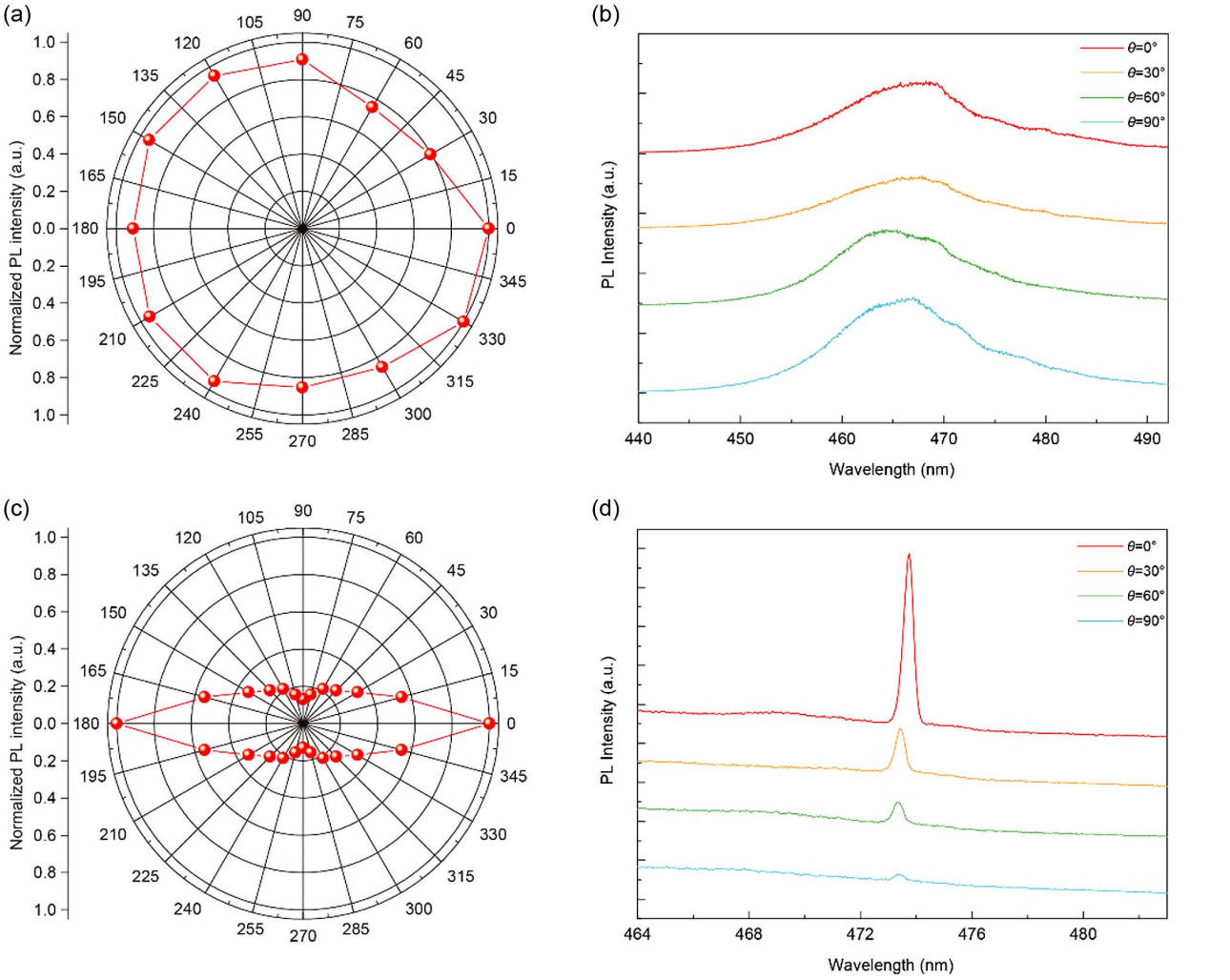

Fig. 3. Polarization properties of $RbPbBr_3$ MCC lasers. (a) Emission spectrum below the lasing threshold ($\approx 0.6P_{th}$) obtained from a single $RbPbBr_3$ MCC under various polarizer rotation angles (θ, in degree). (b) Integrated PL intensity as a function of θ. (c) Emission spectrum above the lasing threshold ($\approx 1.2P_{th}$) obtained from the same $RbPbBr_3$ MCC under various polarizer rotation angles. (d) Integrated lasing peak intensity as a function of θ.

$$R = \frac{I_{max} - I_{min}}{I_{max} + I_{min}}, \quad (3)$$

where I_{max} and I_{min} denote the maximum and minimum lasing emission intensities, respectively. Note that the R value of our laser was determined to be 0.77, which is higher than that of several other lasers [43,44].

D. $Rb_xCs_{1-x}PbBr_3$ MCCs with Wavelength Tunable Emission and High Heat Stability

To achieve a wider range of PL wavelength outputs, Cs^+ was used to replace part of the Rb^+ at the A position of the perovskites. The A-site monovalent cation substitution provided better stability than the traditional mixed halogen modulation of the bandgap. This can be attributed to the fact that halogens are unstable owing to the presence of phase separation effects, whereas A-site cations have larger ionic radii and require much higher ion migration energies for the same effect [45–47]. Typically, the bandgap of $Rb_xCs_{1-x}PbBr_3$ perovskites is determined by the element modulation of the A site, which influences the lattice parameters and bond angles. Here, site cation engineering was achieved by adjusting the Rb/Cs ratio to tune the emission wavelength continuously, covering the green and blue spectra. The PL spectra of $Rb_xCs_{1-x}PbBr_3$ MCCs were recorded at room temperature [Fig. 4(a)], and six strong and narrow peaks at 459, 473, 490, 505, 515, and 525 nm were observed. The PL characteristics of the $Rb_{0.75}Cs_{0.25}PbBr_3$ MCCs at different temperatures are illustrated in Figs. 4(b) and 4(c). To investigate the heat stability, temperature-dependent PL spectra of $CsPbBr_3$ and $Rb_{0.75}Cs_{0.25}PbBr_3$ MCCs were recorded from 293 to 413 K. The PL intensity of the $CsPbBr_3$ MCCs decreased rapidly with increasing temperature, and, as shown in Fig. 4(c), it was 10% at 360 K. Compared with the PL intensity of $CsPbBr_3$, the PL intensity of $Rb_{0.75}Cs_{0.25}PbBr_3$ MCCs decreased more gradually, and it remained at 10% when the temperature increased from 363 to 413 K. This indicates that the $Rb_{0.75}Cs_{0.25}PbBr_3$ demonstrates better heat stability than $CsPbBr_3$ perovskite materials.

Thus, single-mode lasing emission with a high Q-factor and a stable and narrow peak was achieved through element modulation of $Rb_xCs_{1-x}PbBr_3$ MCCs. Tunable single-mode lasing from 468 to 536 nm was realized, as depicted in Fig. 4(d). Although the MCCs were fabricated with a size of approximately 1.2 μm to realize single-mode lasing, the laser line

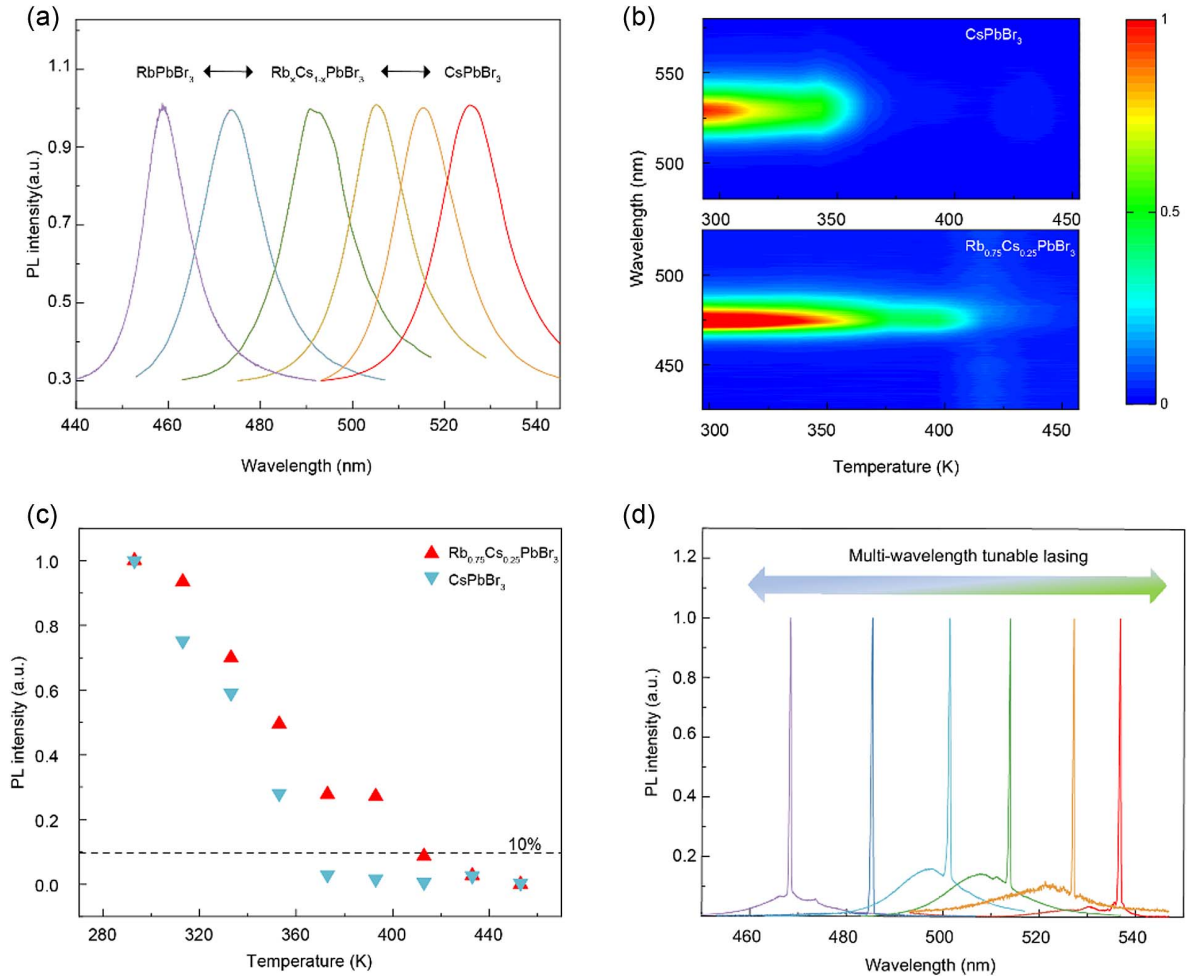

Fig. 4. $Rb_xCs_{1-x}PbBr_3$ MCCs with wavelength tunable emission and high heat stability. (a) PL spectra of $Rb_xCs_{1-x}PbBr_3$ MCCs. (b) Temperature-dependent PL spectra of $CsPbBr_3$ and $Rb_{0.75}Cs_{0.25}PbBr_3$ MCCs. (c) Comparison of the fluorescence intensity for $CsPbBr_3$ (blue) and $Rb_{0.75}Cs_{0.25}PbBr_3$ (red) MCCs with increasing temperature. (d) Single-mode lasing spectra of $Rb_xCs_{1-x}PbBr_3$ MCCs.

width, threshold, and cavity quality factor presented surprisingly good performance.

4. CONCLUSION

In conclusion, we have successfully achieved high-quality blue single-mode lasing in an individual all-inorganic perovskite-phase $RbPbBr_3$ MCC. The perovskite-phase $RbPbBr_3$ MCCs were prepared via one-step chemical vapor deposition. It was found that a high-temperature environment promoted the formation of the perovskite phase and the microcubic morphology of $RbPbBr_3$. The lasing characteristics of our perovskite-phase $RbPbBr_3$ MCCs are remarkable, with a narrow linewidth of ~0.21nm and a high Q-factor of ~2200, which is higher than that of most blue perovskite single-mode lasers reported to date. Additionally, the observed lasing is linearly polarized with a polarization state factor of ~0.77. Furthermore, we have demonstrated the tunability of the mixed-monovalent cation composition, which allowed us to achieve single-mode lasing emission over the blue and green ranges. The heat stability of our perovskite-phase $Rb_xCs_{1-x}PbBr_3$ MCC is better than that of conventional $CsPbBr_3$. Our work has resulted in the development of an outstanding blue single-mode, linearly polarized, and tunable microlaser. We believe that these excellent properties may open up new opportunities for the application of perovskite lasers in blue laser fields and integrated photonic circuits.

Funding. National Natural Science Foundation of China (61675219, 61875256); Natural Science Foundation of Shanghai (20JC1414605).

Disclosures. The authors declare no conflicts of interest.

Data Availability. Data underlying the results presented in this paper are not publicly available at this time but may be obtained from the authors upon reasonable request.

REFERENCES

1. V. D. Ta, R. Chen, L. Ma, Y. J. Ying, and H. D. Sun, "Whispering gallery mode microlasers and refractive index sensing based on single polymer fiber," Laser Photon. Rev. **7**, 133–139 (2013).
2. H. Chang, Y. Zhong, H. Dong, Z. Wang, W. Xie, A. Pan, and L. Zhang, "Ultrastable low-cost colloidal quantum dot microlasers of operative temperature up to 450 K," Light Sci. Appl. **10**, 60 (2021).
3. N. Toropov, G. Cabello, M. P. Serrano, R. R. Gutha, M. Rafti, and F. Vollmer, "Review of biosensing with whispering-gallery mode lasers," Light Sci. Appl. **10**, 42 (2021).
4. Y. Y. Xie, P. N. Ni, Q. H. Wang, Q. Kan, G. Briere, P. P. Chen, Z. Z. Zhao, A. Delga, H. R. Ren, H. D. Chen, C. Xu, and P. Genevet, "Metasurface-integrated vertical cavity surface-emitting lasers for programmable directional lasing emissions," Nat. Nanotechnol. **15**, 125–130 (2020).
5. R. Yan, D. Gargas, and P. Yang, "Nanowire photonics," Nat. Photonics **3**, 569–576 (2009).
6. L. Jin, Z. Liu, Y. Zhang, Y. Wu, Y. Liu, H. Deng, Q. Song, and S. Xiao, "Lanthanide-doped nanocrystals in high-Q microtoroids for stable on-chip white-light lasers," Photon. Res. **10**, 1594–1601 (2022).
7. S. Zhao, Q. Mo, B. Wang, W. Cai, R. Li, and Z. Zang, "Inorganic halide perovskites for lighting and visible light communication," Photon. Res. **10**, 1039–1062 (2022).
8. X. Michalet, F. F. Pinaud, L. A. Bentolila, J. M. Tsay, S. Doose, J. J. Li, G. Sundaresan, A. M. Wu, S. S. Gambhir, and S. Weiss, "Quantum dots for live cells, in vivo imaging, and diagnostics," Science **307**, 538–544 (2005).
9. Z. Qiao, X. Gong, P. Guan, Z. Yuan, S. Feng, Y. Zhang, M. Kim, G.-E. Chang, and Y.-C. Chen, "Lasing action in microdroplets modulated by interfacial molecular forces," Adv. Photon. **3**, 016003 (2021).
10. Y. H. Kim, H. Cho, J. H. Heo, T. S. Kim, N. Myoung, C. L. Lee, S. H. Im, and T. W. Lee, "Multicolored organic/inorganic hybrid perovskite light-emitting diodes," Adv. Mater. **27**, 1248–1254 (2015).
11. L. N. Quan, F. P. Garcia de Arquer, R. P. Sabatini, and E. H. Sargent, "Perovskites for light emission," Adv. Mater. **30**, 1801996 (2018).
12. F. Hao, C. C. Stoumpos, R. P. Chang, and M. G. Kanatzidis, "Anomalous band gap behavior in mixed Sn and Pb perovskites enables broadening of absorption spectrum in solar cells," J. Am. Chem. Soc. **136**, 8094–8099 (2014).
13. A. Kojima, K. Teshima, Y. Shirai, and T. Miyasaka, "Organometal halide perovskites as visible-light sensitizers for photovoltaic cells," J. Am. Chem. Soc. **131**, 6050–6051 (2009).
14. A. Miyata, A. Mitioglu, P. Plochocka, O. Portugall, J. T.-W. Wang, S. D. Stranks, H. J. Snaith, and R. J. Nicholas, "Direct measurement of the exciton binding energy and effective masses for charge carriers in organic–inorganic tri-halide perovskites," Nat. Phys. **11**, 582–587 (2015).
15. D. P. McMeekin, G. Sadoughi, W. Rehman, G. E. Eperon, M. Saliba, M. T. Horantner, A. Haghighirad, N. Sakai, L. Korte, B. Rech, M. B. Johnston, L. M. Herz, and H. J. Snaith, "A mixed-cation lead mixed-halide perovskite absorber for tandem solar cells," Science **351**, 151–155 (2016).
16. G. Xing, N. Mathews, S. S. Lim, N. Yantara, X. Liu, D. Sabba, M. Gratzel, S. Mhaisalkar, and T. C. Sum, "Low-temperature solution-processed wavelength-tunable perovskites for lasing," Nat. Mater. **13**, 476–480 (2014).
17. Z. Liu, J. Yang, J. Du, Z. Hu, T. Shi, Z. Zhang, Y. Liu, X. Tang, Y. Leng, and R. Li, "Robust subwavelength single-mode perovskite nanocuboid laser," ACS Nano **12**, 5923–5931 (2018).
18. B. Tang, H. Dong, L. Sun, W. Zheng, Q. Wang, F. Sun, X. Jiang, A. Pan, and L. Zhang, "Single-mode lasers based on cesium lead halide perovskite submicron spheres," ACS Nano **11**, 10681–10688 (2017).
19. Q. Zhang, R. Su, X. Liu, J. Xing, T. C. Sum, and Q. Xiong, "High-quality whispering-gallery-mode lasing from cesium lead halide perovskite nanoplatelets," Adv. Funct. Mater. **26**, 6238–6245 (2016).
20. Q. Liao, K. Hu, H. Zhang, X. Wang, J. Yao, and H. Fu, "Perovskite microdisk microlasers self-assembled from solution," Adv. Mater. **27**, 3405–3410 (2015).
21. S. Wang, K. Wang, Z. Gu, Y. Wang, C. Huang, N. Yi, S. Xiao, and Q. Song, "Solution-phase synthesis of cesium lead halide perovskite microrods for high-quality microlasers and photodetectors," Adv. Opt. Mater. **5**, 1700023 (2017).
22. H. Zhu, Y. Fu, F. Meng, X. Wu, Z. Gong, Q. Ding, M. V. Gustafsson, M. T. Trinh, S. Jin, and X.-Y. Zhu, "Lead halide perovskite nanowire lasers with low lasing thresholds and high quality factors," Nat. Mater. **14**, 636–642 (2015).
23. Z. Hu, Z. Liu, Z. Zhan, T. Shi, J. Du, X. Tang, and Y. Leng, "Advances in metal halide perovskite lasers: synthetic strategies, morphology control, and lasing emission," Adv. Photon. **3**, 034002 (2021).
24. L. Zhang and R. Long, "Developments and challenges ahead in blue perovskite light-emitting devices," J. Energy Chem. **71**, 418–433 (2022).
25. L. Cheng, C. Yi, Y. Tong, L. Zhu, G. Kusch, X. Wang, X. Wang, T. Jiang, H. Zhang, J. Zhang, C. Xue, H. Chen, W. Xu, D. Liu, R. A. Oliver, R. H. Friend, L. Zhang, N. Wang, W. Huang, and J. Wang, "Halide homogenization for high-performance blue perovskite electroluminescence," Research **2020**, 9017871 (2020).
26. J. M. Pina, D. H. Parmar, G. Bappi, C. Zhou, H. Choubisa, M. Vafaie, A. M. Najarian, K. Bertens, L. K. Sagar, Y. Dong, Y. Gao, S. Hoogland, M. I. Saidaminov, and E. H. Sargent, "Deep-blue perovskite single-mode lasing through efficient vapor-assisted chlorination," Adv. Mater. **33**, 2006697 (2021).
27. M. Karlsson, Z. Yi, S. Reichert, X. Luo, W. Lin, Z. Zhang, C. Bao, R. Zhang, S. Bai, G. Zheng, P. Teng, L. Duan, Y. Lu, K. Zheng, T. Pullerits, C. Deibel, W. Xu, R. Friend, and F. Gao, "Mixed halide

perovskites for spectrally stable and high-efficiency blue light-emitting diodes," Nat. Commun. **12**, 361 (2021).
28. M. Lai, A. Obliger, D. Lu, C. S. Kley, C. G. Bischak, Q. Kong, T. Lei, L. Dou, N. S. Ginsberg, D. T. Limmer, and P. Yang, "Intrinsic anion diffusivity in lead halide perovskites is facilitated by a soft lattice," Proc. Natl. Acad. Sci. USA **115**, 11929–11934 (2018).
29. L. Chen, B. Zhou, Y. Hu, H. Dong, G. Zhang, Y. Shi, and L. Zhang, "Stable multi-wavelength lasing in single perovskite quantum dot superlattice," Adv. Opt. Mater. **10**, 2200494 (2022).
30. Y. Dong, Y.-K. Wang, F. Yuan, A. Johnston, Y. Liu, D. Ma, M.-J. Choi, B. Chen, M. Chekini, S.-W. Baek, L. K. Sagar, J. Fan, Y. Hou, M. Wu, S. Lee, B. Sun, S. Hoogland, R. Quintero-Bermudez, H. Ebe, P. Todorovic, F. Dinic, P. Li, H. T. Kung, M. I. Saidaminov, E. Kumacheva, E. Spiecker, L.-S. Liao, O. Voznyy, Z.-H. Lu, and E. H. Sargent, "Bipolar-shell resurfacing for blue LEDs based on strongly confined perovskite quantum dots," Nat. Nanotechnol. **15**, 668–674 (2020).
31. C. Xu, X. Chen, S. Ma, M. Shi, S. Zhang, Z. Xiong, W. Fan, H. Si, H. Wu, Z. Zhang, Q. Liao, W. Yin, Z. Kang, and Y. Zhang, "Interpretation of rubidium-based perovskite recipes toward electronic passivation and ion-diffusion mitigation," Adv. Mater. **34**, 2109998 (2022).
32. O. A. Syzgantseva, M. Saliba, M. Grätzel, and U. Rothlisberger, "Stabilization of the perovskite phase of formamidinium lead triiodide by methylammonium, Cs, and/or Rb doping," J. Phys. Chem. Lett. **8**, 1191–1196 (2017).
33. M. Saliba, T. Matsui, K. Domanski, J.-Y. Seo, A. Ummadisingu, S. M. Zakeeruddin, J.-P. Correa-Baena, W. R. Tress, A. Abate, A. Hagfeldt, and M. Grätzel, "Incorporation of rubidium cations into perovskite solar cells improves photovoltaic performance," Science **354**, 206–209 (2016).
34. H. Kim, H. R. Byun, and M. S. Jeong, "Synthesis and characterization of multiple-cation Rb(MAFA)PbI_3 perovskite single crystals," Sci. Rep. **9**, 2022 (2019).
35. B. Tang, Y. Hu, H. Dong, L. Sun, B. Zhao, X. Jiang, and L. Zhang, "An all-inorganic Perovskite-phase rubidium lead bromide nanolaser," Angew. Chem. **131**, 16280–16286 (2019).
36. Z. L. Wang, "Transmission electron microscopy of shape-controlled nanocrystals and their assemblies," J. Phys. Chem. B **104**, 1153–1175 (2000).
37. B. Zhou, H. Dong, M. Jiang, W. Zheng, L. Sun, B. Zhao, B. Tang, A. Pan, and L. Zhang, "Single-mode lasing and 3D confinement from perovskite micro-cubic cavity," J. Mater. Chem. C **6**, 11740–11748 (2018).
38. M. Borselli, T. J. Johnson, and O. Painter, "Beyond the Rayleigh scattering limit in high-*Q* silicon microdisks: theory and experiment," Opt. Express **13**, 1515–1530 (2005).
39. S. Yang, Y. Wang, and H. Sun, "Advances and prospects for whispering gallery mode microcavities," Adv. Opt. Mater. **3**, 1136–1162 (2015).
40. G.-Q. Wei, Y. Yu, M.-P. Zhuo, X.-D. Wang, and L.-S. Liao, "Organic single-crystalline whispering-gallery mode microlasers with efficient optical gain activated via excited state intramolecular proton transfer luminogens," J. Mater. Chem. C **8**, 11916–11921 (2020).
41. W. Du, X. Wu, S. Zhang, X. Sui, C. Jiang, Z. Zhu, Q. Shang, J. Shi, S. Yue, Q. Zhang, J. Zhang, and X. Liu, "All optical switching through anistropic gain of $CsPbBr_3$ single crystal microplatelet," Nano Lett. **22**, 4049–4057 (2022).
42. J. Hu, L.-S. Li, W. Yang, L. Manna, L.-W. Wang, and A. P. Alivisatos, "Linearly polarized emission from colloidal semiconductor quantum rods," Science **292**, 2060–2063 (2001).
43. M. Rashidi, T. Haggren, C. Jagadish, and H. H. Tan, "Characteristics and thermal control of random and Fabry–Pérot lasing in nanowire arrays," ACS Photon. **9**, 3573–3583 (2022).
44. M. Sak, N. Taghipour, S. Delikanli, S. Shendre, I. Tanriover, S. Foroutan, Y. Gao, J. Yu, Z. Yanyan, S. Yoo, C. Dang, and H. V. Demir, "Coreless fiber-based whispering-gallery-mode assisted lasing from colloidal quantum well solids," Adv. Funct. Mater. **30**, 1907417 (2019).
45. D. Lin, T. Shi, H. Xie, F. Wan, X. Ren, K. Liu, Y. Zhao, L. Ke, Y. Lin, Y. Gao, X. Xu, W. Xie, P. Liu, and Y. Yuan, "Ion migration accelerated reaction between oxygen and metal halide perovskites in light and its suppression by cesium incorporation," Adv. Energy Mater. **11**, 2002552 (2021).
46. D. W. Ferdani, S. R. Pering, D. Ghosh, P. Kubiak, A. B. Walker, S. E. Lewis, A. L. Johnson, P. J. Baker, M. S. Islam, and P. J. Cameron, "Partial cation substitution reduces iodide ion transport in lead iodide perovskite solar cells," Energy Environ. Sci. **12**, 2264–2272 (2019).
47. X. Wang, Y. Ling, X. Lian, Y. Xin, K. B. Dhungana, F. Perez-Orive, J. Knox, Z. Chen, Y. Zhou, D. Beery, K. Hanson, J. Shi, S. Lin, and H. Gao, "Suppressed phase separation of mixed-halide perovskites confined in endotaxial matrices," Nat. Commun. **10**, 695 (2019).